AIAA 2002-4505

Aeroheating Environments for a Mars Smart Lander

Karl T. Edquist, Derek S. Liechty, Brian R. Hollis, and Stephen J. Alter

NASA Langley Research Center
Hampton, VA

Mark P. Loomis

NASA Ames Research Center
Moffett Field, CA

AIAA Atmospheric Flight Mechanics Conference & Exhibit

5-8 August, 2002
Monterey, California

AEROHEATING ENVIRONMENTS FOR A
MARS SMART LANDER

Karl T. Edquist*, Derek S. Liechty[†], Brian R. Hollis[‡], and Stephen J. Alter[§]
NASA Langley Research Center
Hampton, VA

Mark P. Loomis[¶]
NASA Ames Research Center
Moffett Field, CA

ABSTRACT

A proposed Mars Smart Lander is designed to reach the surface via lifting-body atmospheric entry ($\alpha = 16$ *deg*) to within 10 *km* of the target site. CFD predictions of the forebody aeroheating environments are given for a direct entry from a 2005 launch. The solutions were obtained using an 8-species gas in thermal and chemical non-equilibrium with a radiative-equilibrium wall temperature boundary condition. Select wind tunnel data are presented from tests at NASA Langley Research Center. Turbulence effects are included to account for both smooth body transition and turbulence due to heatshield penetrations. Natural transition is based on a momentum-thickness Reynolds number value of 200. The effects of heatshield penetrations on turbulence are estimated from wind tunnel tests of various cavity sizes and locations. Both natural transition and heatshield penetrations are predicted to cause turbulence prior to the nominal trajectory peak heating time. Laminar and turbulent CFD predictions along the trajectory are used to estimate heat rates and loads. The predicted peak turbulent heat rate of 63 *W/cm²* on the heatshield leeward flank is 70% higher than the laminar peak. The maximum integrated heat load for a fully turbulent heat pulse is 38% higher than the laminar load on the heatshield nose. The predicted aeroheating environments with uncertainty factors will be used to design a thermal protection system.

NOMENCLATURE

C_D	drag coefficient, $D/\frac{1}{2}\rho_\infty V_\infty^2 S$
D	heatshield diameter (*m*)
h	altitude (*km*)
L/D	lift-to-drag ratio
m	aeroshell mass (*kg*)
p	pressure (*N/m²*)
Q	heat load (*J/cm²*)
q	heat rate (*W/cm²*)
R	heatshield radius (*m*)
R_n	nose radius (*m*)
R_s	shoulder radius (*m*)
Re	Reynolds number
r	radial coordinate (*m*)
S	reference area, $\pi D^2/4$ (*m²*)
s	running length (*m*)
T	temperature (*K*)
TPS	Thermal Protection System
t	time from atmospheric interface (*s*)
u	velocity parallel to surface (*m/s*)
V	velocity (*km/s*)
W	full-scale heatshield cavity diameter (*in*)
x	radial coordinate (*m*)
y^+	non-dimensional boundary layer coordinate
α	trim angle of attack (*deg*)
β_m	ballistic coefficient, $m/C_D S$ (*kg/m²*)
δ	boundary layer thickness (*in*)
ϕ	circumferential location on heatshield measured clockwise from leeside (*deg*)
γ	flight path angle (*deg*)
μ	viscosity (*kg/m²-s*)
θ	momentum thickness (*m*)
θ_c	cone half angle (*deg*)
ρ	density (*kg/m³*)
ξ_{max}	maximum grid stretching in the surface normal coordinate direction

Subscripts

D	heatshield diameter
e	boundary layer edge
FR	Fay-Riddell value
lam	laminar
$turb$	turbulent
w	wall
θ	momentum thickness
∞	freestream

* Vehicle Analysis Branch, Senior Member, AIAA.
[†] Aerothermodynamics Branch.
[‡] Aerothermodynamics Branch, Senior Member, AIAA.
[§] Aerothermodynamics Branch, Senior Member, AIAA.
[¶] Reacting Flow Environments Branch, Member, AIAA.

INTRODUCTION

First generation Mars landers such as Viking and Pathfinder successfully used entry trajectories that provided landing accuracy within hundreds of kilometers of their targets. Second generation landers are characterized by their ability for precise landing (< 10 *km*) near areas that are of particular scientific interest[1]. The Mars Smart Lander (MSL) is a proposed mission that is designed to achieve precise landing accuracy at sites that were previously unreachable.

Figure 1 shows a proposed MSL configuration in which the cruise stage is attached to the lander pallet through the heatshield. The rover occupies much of the interior volume and requires a larger backshell than was used for Viking and Pathfinder. The aeroshell is designed to separate from the cruise stage prior to atmospheric interface and then deliver the lander to the Martian surface.
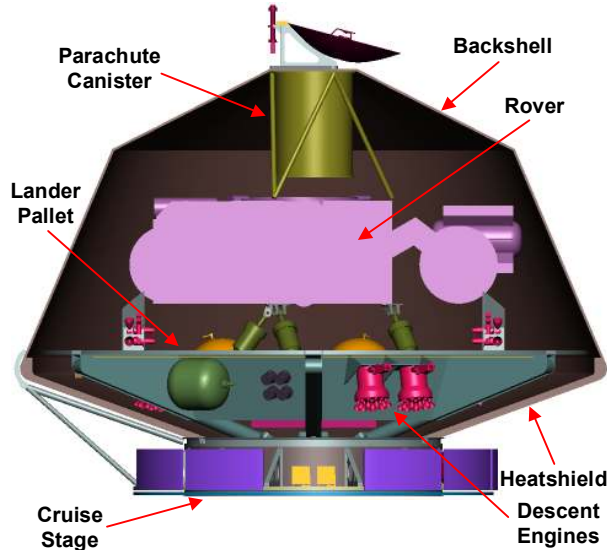

Figure 1. MSL Cruise Configuration

A guided lifting-body entry is proposed for MSL to achieve 10-*km* landing accuracy. The entry vehicle lift is used to mitigate uncertainties in predicted entry states, atmospheric properties, aerodynamics, etc. that would otherwise contribute to large landing footprints. A hypersonic lift-to-drag ratio (*L/D*) of 0.22-0.25 and ballistic coefficient (β_m) less than 120 kg/m^2 meet the delivery requirements for a direct entry from the 2005 launch opportunity.

The aeroshell contents will require protection from exposure to significant aerothermal environments during entry. Knowledge of the expected heating is necessary for proper design of the thermal protection system (TPS). This paper summarizes the predicted forebody aeroheating environments for the proposed MSL mission using a combination of CFD calculations and wind tunnel data.

Heatshield Geometry

The heatshield geometry used for the aeroheating predictions is a 4.05-*m* diameter, 70-*deg* half-angle sphere-cone shown in Figure 2. Table 1 summarizes the heatshield dimensions. The forebody geometry is similar to that of Pathfinder, but much larger (4.05 *m* vs. 2.65 *m*). A stable trim angle of 16 *deg* is required for hypersonic *L/D* = 0.22-0.25 and is achieved with a radial center-of-gravity offset.
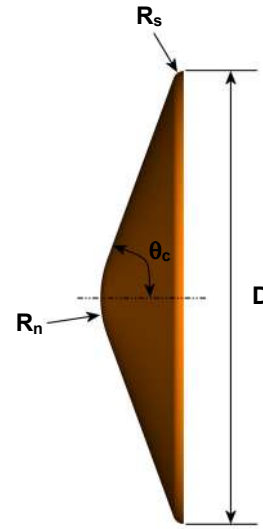

Figure 2. Heatshield Geometry

Table 1. Heatshield Dimensions

Parameter	Dimension
D (*m*)	4.05
θ_c (*deg*)	70
R_n (*m*)	0.9854
R_s (*m*)	0.0988

Heatshield Penetrations

If the entry vehicle is attached to the cruise stage through the heatshield, cavities will remain after cruise stage separation. Figure 3 shows six equally spaced cavities of diameter *W* at radial location *r* that are left behind when the bolts connecting the pallet and cruise ring are severed. The cavity depth is expected to be smaller than the diameter. The cavities could significantly augment the heating environment in the vicinity of the penetrations and downstream. A combination of CFD and wind tunnel test data was used to investigate the penetration effects on aeroheating.

Figure 3. Lander Pallet/Cruise Stage Attachment Points through Heatshield

Nominal Entry Trajectory

Aeroheating environments analysis requires knowledge of the entry trajectory and associated heat pulse. Trajectories for the 2005 launch opportunity were calculated using the Program to Optimize Simulated Trajectories (POST)[2]. A total of 2000 three degree-of-freedom Monte-Carlo simulations was performed to investigate dispersions in entry states, atmospheric properties, and aerodynamics, among others. The nominal, or expected, entry trajectory was selected for initial aeroheating analysis. A velocity of 5.56 *km/s* and flight path angle of –12.5 *deg* at atmospheric interface produce the velocity-altitude map shown in Figure 4. Peak stagnation point heating occurs at an altitude of 37.1 *km* and a velocity of 4.92 *km/s*. CFD predictions of the heatshield aeroheating environments are shown for the nominal trajectory.

Figure 4. Nominal Entry Trajectory for the 2005 Launch Opportunity

ANALYSIS

Computational Approach

CFD calculations at flight conditions were performed using the Langley Aerothermodynamic Upwind Relaxation Algorithm (LAURA)[3] and General Aerodynamics Simulation Program (GASP)[4] CFD codes. Both codes were exercised using an 8-species Mars gas (CO_2, CO, N_2, O_2, NO, C, N, O) in thermal and chemical non-equilibrium with a radiative-equilibrium wall temperature boundary condition. The Park-94[5] reaction rates were used for the 8-species chemistry model in both codes. A "super-catalytic" wall boundary condition was used in which the species mass fractions for CO_2 and N_2 are fixed at their freestream values of 0.97 and 0.03, respectively. This assumption gives the most conservative heating levels. LAURA was used for a series of aeroheating predictions along the nominal trajectory and GASP was used to support those results. Only convective heating is predicted because the contribution from radiation should be negligible.

LAURA CFD Code

LAURA was developed at NASA Langley Research Center (LaRC) and has been used previously to predict the aeroheating environments for various Mars projects[6,7]. The code uses a finite-volume approach to solve the inviscid, thin-layer Navier-Stokes (TLNS), or full Navier-Stokes flowfield equations. The TLNS option was used for all LAURA calculations presented here. Roe's averaging[8] is used for the inviscid fluxes with second-order corrections using Yee's symmetric total variation diminishing (TVD) scheme[9]. Turbulent LAURA solutions were obtained using the Baldwin-Lomax algebraic model[10,11]. On a simple sphere-cone geometry, the Baldwin-Lomax model is believed to give reasonable results. A user-specified transition location is required to run the model and was specified to give fully turbulent results for conservatism.

A built-in LAURA grid alignment capability allows mesh adaptation to the boundary layer and bow shock according to user-defined parameters. Proper cell spacing at the wall is important for heating calculations and is controlled in LAURA by the wall cell Reynolds number, which is defined as:

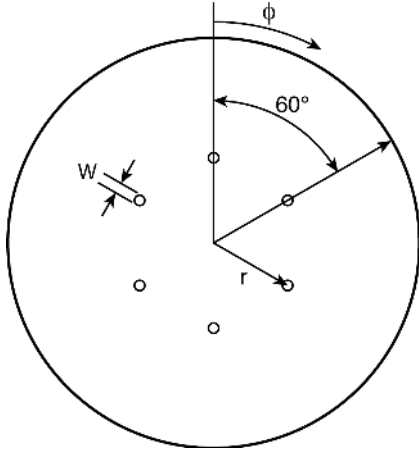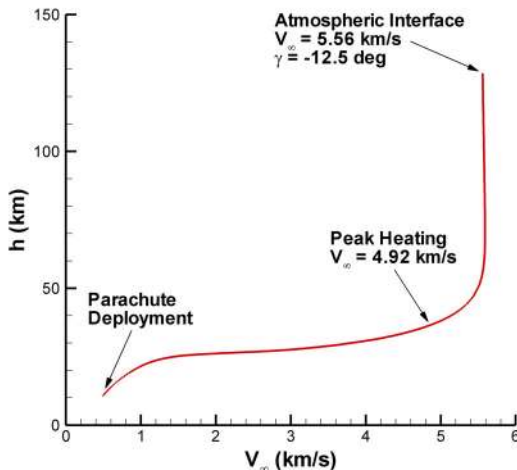$$Re_w = \left(\frac{\rho a \Delta \eta}{\mu} \right)_w \qquad (1)$$

American Institute of Aeronautics and Astronautics

where ρ is the density, a is the speed of sound, $\Delta\eta$ is the cell height, and μ is the viscosity. The author's experience is that reliable laminar heating predictions can be achieved using $Re_w = 10$. A Re_w value of 2 was used for turbulent calculations to give a y^+ value of order 0.1, where y^+ is defined as:

$$y^+ = \frac{\eta\rho}{\mu}\sqrt{\frac{\tau_w}{\rho}} \qquad (2)$$

The quantities η and τ_w are the surface normal distance and shear stress, respectively.

GASP CFD Code

GASP has been used extensively at NASA Ames Research Center in TPS sizing applications for both planetary[12,13] and transatmospheric[14] entry vehicles. The GASP solutions were run with models that are similar, if not identical, to those used in LAURA. The transport properties are calculated with Wilke's[15] mixing rule with curve fits for the species viscosities given by Blottner, et al.[16] and Eucken's[17] correlation for thermal conductivity. Binary diffusion was used with a constant Schmidt number of 0.7, which indicates the ratio of momentum and mass diffusivities. The Van Leer[18] flux splitting scheme with the min-mod limiter is used to calculate the inviscid fluxes and a central-difference approximation is used for the viscous fluxes. For turbulent calculations, the Baldwin-Lomax model was used with a compressibility correction.

Computational Grid

A 7-block, singularity-free, structured volume grid was used for the LAURA solutions. The heatshield nose was meshed to avoid a singularity pole boundary because it can introduce discontinuities in the flowfield solution. Figure 5 shows the surface and symmetry plane grid distributions coarsened by a factor of two in each direction. Only half of the heatshield is modeled due to symmetry in the pitch plane. The grid was built using GridGen[19] to construct the topology and surface distribution, 3DGRAPE/AL[20] to generate the volume grid, and the Volume Grid Manipulator (VGM)[21] to enhance grid quality and accurately impose boundary conditions along block interfaces.

A total of 3280 surface and 64 normal cells was used to resolve the flowfield. The circumferential mesh distribution is equally spaced at 3-*deg* increments for a total of 60 cells. A relatively fine streamwise grid distribution is used on the nose and shoulder to accurately reproduce the surface geometry and capture steep flowfield gradients in those regions.
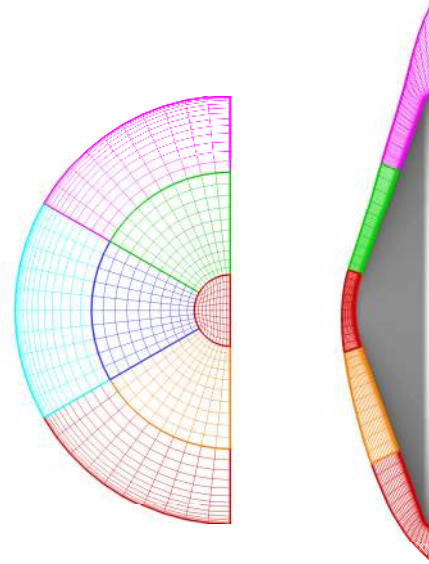

Figure 5. Heatshield Surface and Symmetry Plane Grids Used for LAURA Solutions (Coarsened)

CFD Solution Points

Detailed aeroheating environments prediction at flight conditions requires high-fidelity CFD calculations at multiple points along the design trajectory. Figure 6 shows 12 points on the 2005 nominal trajectory at which LAURA solutions were obtained. Some points were identified to analyze specific milestones, such as peaks in stagnation point heating ($t = 103$ s), dynamic pressure ($t = 119$ s), and Reynolds number ($t = 130$ s). The remaining points were selected to fill out the heat pulse with sufficient resolution. The heat rate shown in Figure 6 is based on the Fay-Riddell formula[22] and is not corrected for angle-of-attack. The entire heat pulse lasts about five minutes, with most of the heating occurring at $t = 45$-190 s.
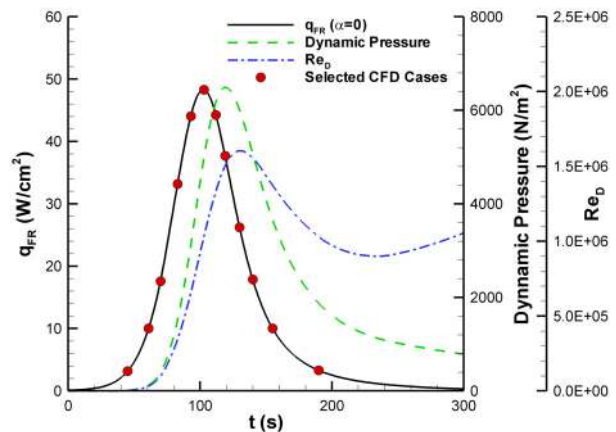

Figure 6. CFD Solution Points along Nominal Trajectory

Table 2 summarizes the freestream conditions for the CFD solutions. All flight cases were run at $\alpha = 16\ deg$, which is required for a hypersonic $L/D = 0.22$-0.25.

Table 2. Freestream Conditions for CFD Solutions

t (s)	h (km)	V_∞ (km/s)	ρ_∞ (kg/m^3)	T_∞ (K)
45	80.6	5.59	8.31 x 10^{-7}	108.8
61	66.2	5.59	8.26 x 10^{-6}	116.1
70	58.9	5.58	2.59 x 10^{-5}	120.2
83	49.2	5.48	1.02 x 10^{-4}	133.4
93	42.6	5.28	2.26 x 10^{-4}	147.5
103	37.1	4.92	4.15 x 10^{-4}	159.3
112	33.3	4.47	6.20 x 10^{-4}	167.6
119	31.1	4.07	7.82 x 10^{-4}	170.5
130	28.8	3.47	9.99 x 10^{-4}	173.6
140	27.5	2.98	1.14 x 10^{-3}	175.3
155	26.7	2.42	1.24 x 10^{-3}	176.5
190	25.6	1.64	1.39 x 10^{-3}	178.1

Experimental Approach

Tests were conducted in NASA LaRC's 20-Inch Mach 6 Air Tunnel to investigate the aeroheating characteristics of various proposed MSL configurations. The test objectives were to compare the heating environments on different geometries and determine the effects of heatshield penetrations on turbulent transition and heating augmentation. Table 3 lists the pertinent test parameters. A range of Reynolds numbers (Re_∞), angles-of-attack, and cavity diameters and locations was investigated. References 23-25 contain detailed discussions of the aeroheating test objectives and results. Reference 25 also includes heating data on asymmetric heatshield shapes.

Table 3. Aeroheating Test Parameters

Parameter	Value
Model Diameter (*in*)	5 (3.1 % scale)
Mach number	6
Reynolds number	2.6 - 7.3 x 10^6 / *ft*
Angle of attack (*deg*)	0, 11, 16, 20
Cavity Diameter, W (*in*)	1, 2.2, 3 (full scale)
Cavity Depth (*in*)	0.3W
Cavity Location (r/R)	0.41, 0.7

Global surface heating distributions were obtained on ceramic models using the two-color, relative-intensity, phosphor thermography method[26,27]. Phosphor thermography is the standard method at LaRC for obtaining global surface heating in the center's hypersonic tunnels. Heating on complex three-

dimensional shapes can be collected with less cost and lead-time requirements than with discrete gauges.

A test model with cavities is shown in Figure 7. During a tunnel run, the phosphor-coated model fluoresces under ultraviolet light according to surface temperature. Model temperature before and after a run is digitized and reduced to a heat rate using one-dimensional heat conduction theory. The total experimental uncertainty is estimated to be +/- 13% for the conical flank. This estimate takes into account uncertainties in freestream conditions, fluorescent intensity, data extraction, and model conduction.
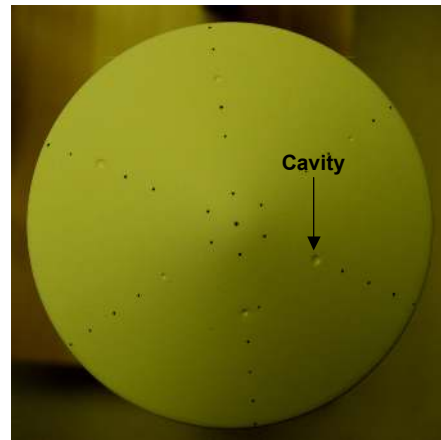

Figure 7. Phosphor-Coated Tunnel Model with Six Cavities (Black Dots are Fiducial Marks)

RESULTS AND DISCUSSION

Laminar and turbulent CFD flight predictions are presented for the nominal trajectory from a 2005 launch. The laminar results were used for the transition analysis and the turbulent cases provide estimates of turbulent heating augmentation.

Transition to Turbulence

Transition via two mechanisms was analyzed for the MSL heatshield with penetrations: natural smooth body transition due to boundary layer instabilities and tripped turbulence caused by heatshield cavities. Surface roughness and ablation product effects on transition have not yet been analyzed and are a function of the TPS material.

Smooth Body Transition

The prediction of natural turbulent transition in the hypersonic regime is an ongoing effort[28,29]. The influence of boundary layer instabilities on turbulence is not well known and is a function of many parameters

that are unique to a given configuration and flow conditions. A known fact, which has been observed repeatedly, is that turbulence occurs more readily with increasing Reynolds number. One common method of predicting transition, which is based on a constant momentum-thickness Reynolds number (Re_θ), was used to analyze turbulent transition for the MSL heating environments. The definition of Re_θ is based on the boundary layer edge properties and momentum thickness (θ), which is a measure of the momentum deficit due to the boundary layer:

$$Re_\theta = \frac{\rho_e u_e \theta}{\mu_e} \qquad (3)$$

$$\theta = \int_0^\infty \frac{\rho u}{\rho_e u_e}\left(1 - \frac{u}{u_e}\right) d\eta \qquad (4)$$

The boundary layer edge is defined as the location where total enthalpy is 99.5% of the freestream value.

The trim angle of 16 *deg* has strong implications for the stagnation point location and propensity for turbulent transition. The streamlines in the symmetry plane and near the surface are plotted with non-dimensional pressure at the nominal trajectory peak heating point in Figure 8. At $\alpha = 16$ *deg*, the stagnation point moves off the heatshield nose and onto the bottom (windward) flank. This stagnation point location results in a short boundary layer running length on the windward side and, more importantly, a long running length on the top (leeward) side. Boundary layer instabilities are more likely to occur when a long running length exists.
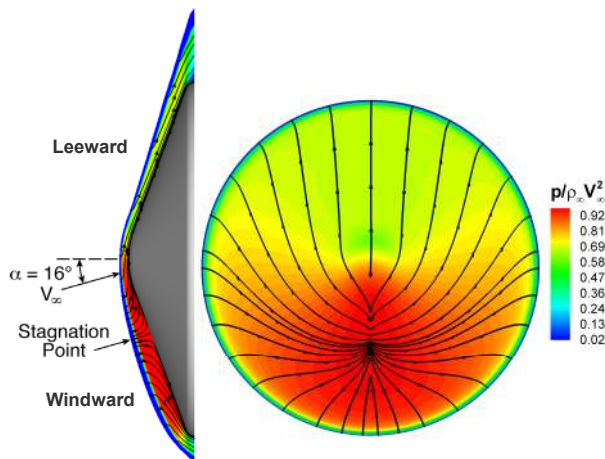
Figure 8. LAURA Symmetry Plane and Surface Pressure and Streamlines at Nominal Peak Heating ($\alpha = 16$ *deg*)

A conservative transition criterion of $Re_\theta > 200$ was used for MSL and is based on previous experience with hypersonic blunt bodies[30]. The effect of the trim angle on the boundary layer is shown in Figure 9. Non-dimensional surface pressure is plotted with $Re_\theta = 200$ and boundary layer edge Mach number ($M_e = 1$) at the nominal trajectory peak heating point. Based on the transition criterion, turbulence is predicted for most of the leeward side of the heatshield, where running length and edge velocity are largest. In contrast, turbulence is not predicted for the windward side of the heatshield. A subsonic boundary layer exists on most of the heatshield and may promote transition in the presence of surface roughness and/or mass addition from ablation products.
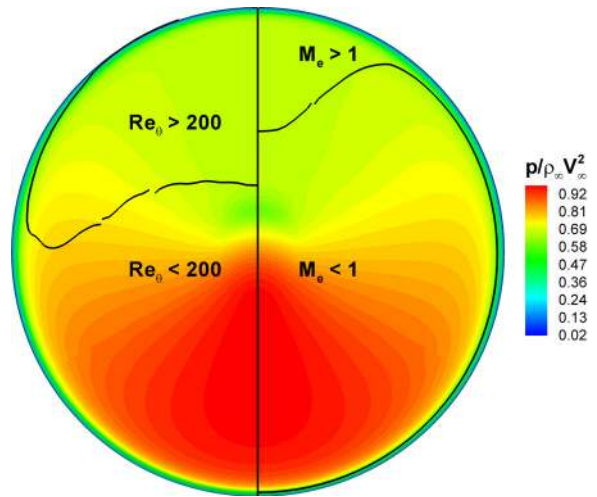
Figure 9. LAURA Surface Pressure, $Re_\theta = 200$, and $M_e = 1$ at Nominal Peak Heating ($\alpha = 16$ *deg*)

Figure 10 shows LAURA laminar symmetry plane Re_θ distributions at select times along the nominal trajectory. The peak Re_θ values are plotted as a function of time with freestream dynamic pressure in Figure 11. The Re_θ values are highest on the leeward flank where the running length and edge velocity are large; the lowest magnitudes are located on the windward side near the stagnation point. Note that Re_θ closely follows dynamic pressure and their peak values occur at the same time. Transition is predicted slightly before $t = 83$ *s* on the leeward side, but never on the windside. Since transition is predicted before the peak heating time, turbulent augmentation will be shown to have a significant effect on the peak heat rate and integrated heat load delivered to the heatshield.
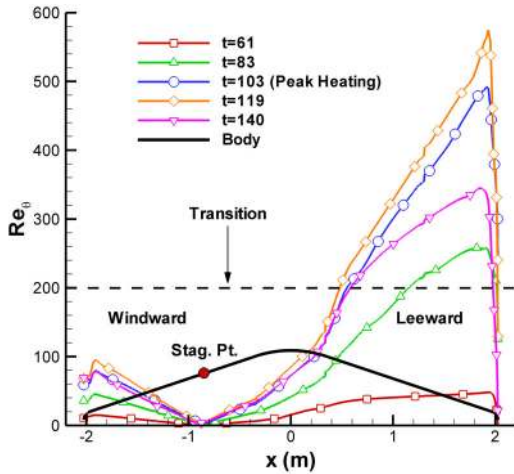
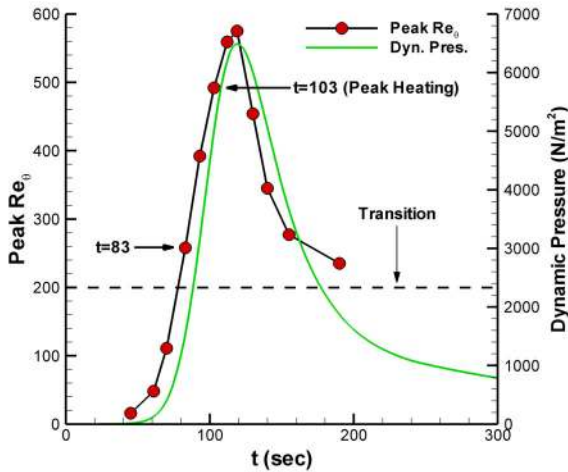**Figure 10. LAURA Symmetry Plane Re_θ along Nominal Trajectory (α = 16 *deg*)**

Figure 11. LAURA Peak Re_θ and Freestream Dynamic Pressure along Nominal Trajectory (α = 16 *deg*)

It should be noted that the Re_θ transition criterion was originally developed with engineering boundary layer codes. It has been observed that the boundary layer edge properties predicted by CFD and engineering codes can differ significantly. The result is that CFD codes often predict higher Re_θ values (by a factor of 2) than do engineering codes, and thus have some built-in conservatism. However, even if the MSL Re_θ transition criterion was doubled to 400 to account for conservative CFD results, transition would still be predicted before the peak heating time. Also, a Re_θ value of 200 seems reasonable at this time since turbulence due to surface roughness and mass addition from ablation products have not yet been considered.

Heatshield Penetrations

The existence of heatshield cavities may also cause turbulence and augment heating. Heatshield penetrations are being used for the Genesis Sample Return Capsule (SRC); CFD and wind tunnel data were used to predict the influence of the cavities on aeroheating[31]. The same approach is used for MSL in which the penetration effects are reduced to a function of the penetration size (*W*), local boundary layer thickness (δ), and Re_θ. CFD and tunnel data were used to predict combinations of penetration configurations and flowfield conditions that result in a tripped turbulent boundary layer and augmented heating. Table 4 lists the various cavity sizes and locations tested on 3.1% scale models in the LaRC 20-Inch Mach 6 Air Tunnel.

Table 4. Aeroheating Test Heatshield Cavity Parameters

Cavity	*W* (*in*, full scale)	*r/R*
1	3.0	0.7
2	2.2	0.7
3	1.5	0.7
4	3.0	0.41
5	2.2	0.41
6	1.5	0.41

In general, larger cavities at higher freestream Reynolds numbers (Re_∞), and thus higher Re_θ, are more likely to trip the boundary layer. The effect of Re_∞ on the penetration's ability to cause turbulence is shown in Figure 12. The family of curves represent heat rate profiles behind a leeside 2.2-*in* penetration (on a 4.05 *m* aeroshell) for various Re_∞ at α = 16 *deg*. The auxiliary figures show the cavity locations and phosphor thermography results at the highest Re_∞ (7.3 x 10^6 / *ft*); all but cavity number 2 increases the heating in wedge-shaped regions behind the penetrations.

For a low Re_∞ (3.0 x 10^6 / *ft*), the heating behind cavity 5 is the same as the laminar smooth body level. With increasing Re_∞, the cavity is more effective in causing turbulence and augmenting the downstream heating. At the highest Re_∞ (7.3 x 10^6 / *ft*), the heating asymptotically reaches a non-dimensional turbulent level of q_{turb}/q_{FR} = 1.08, compared to a peak laminar nose value of approximately q_{lam}/q_{FR} = 0.73. Thus, the laminar heat rate is increased by approximately 48% due to cavity-induced turbulence. If similar heating augmentation exists in flight, the TPS requirements can increase significantly.
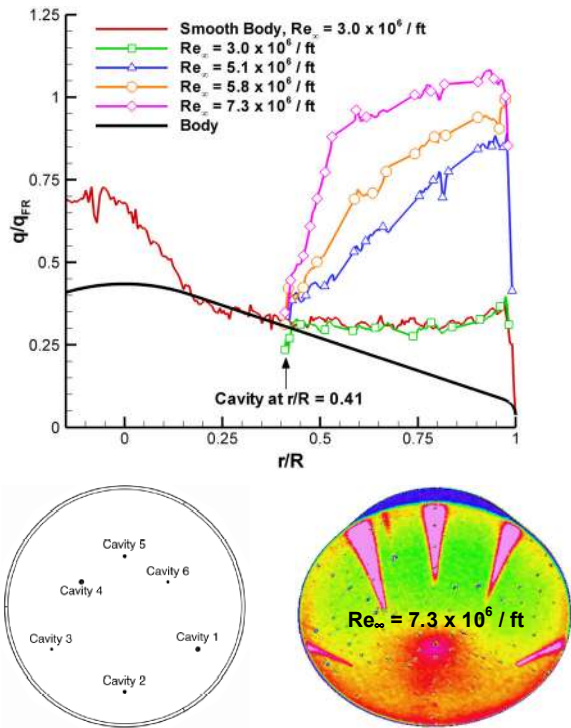
7
American Institute of Aeronautics and Astronautics

Figure 12. Heat Rate Data for Symmetry Plane Cavity #5 ($\phi = 0$) at Various Re_∞ ($\alpha = 16$ *deg*)

The *transition map* in Figure 13 assembles all combinations of cavity size and location, Re_∞, and α from the aeroheating tests into a comprehensive plot showing the penetration effects on turbulent transition. The plot of Re_θ vs. W/δ is divided into regions of *laminar, local disturbance, transitional*, and *turbulent* heating levels based on the tunnel data. The legend shows representative heating images for the different data groups. The Re_θ and δ values for each point were computed with LAURA at tunnel conditions assuming perfect gas and a constant wall temperature of 300 K. Some overlap exists between adjacent data groups and may be due to the fact that data from all angles-of-attack (0–20 *deg*) are placed on the same plot. Curve fits of the data were used to delineate the regions of the map and predict the penetration effects in flight. Conservative design practice would mandate using the *laminar boundary* curve as the transition indicator. See Reference 20 for a discussion of the transition map development.

Values of Re_θ and W/δ were calculated for a 3-*in* leeside penetration ($r/R = 0.41$, $\phi = 0$) along the 2005 nominal trajectory. Based on these calculations, it is estimated that the penetration would trip the boundary layer to full turbulence between $t = 83$ *s* and $t = 93$ *s*, which is well before the peak heating point at $t = 103$ *s*. The smooth body transition analysis also indicated a transition time near $t = 83$ *s*. Therefore, flight

predictions should be made using turbulent solutions by at least $t = 83$ *s* on the nominal trajectory to properly estimate the heating environments.
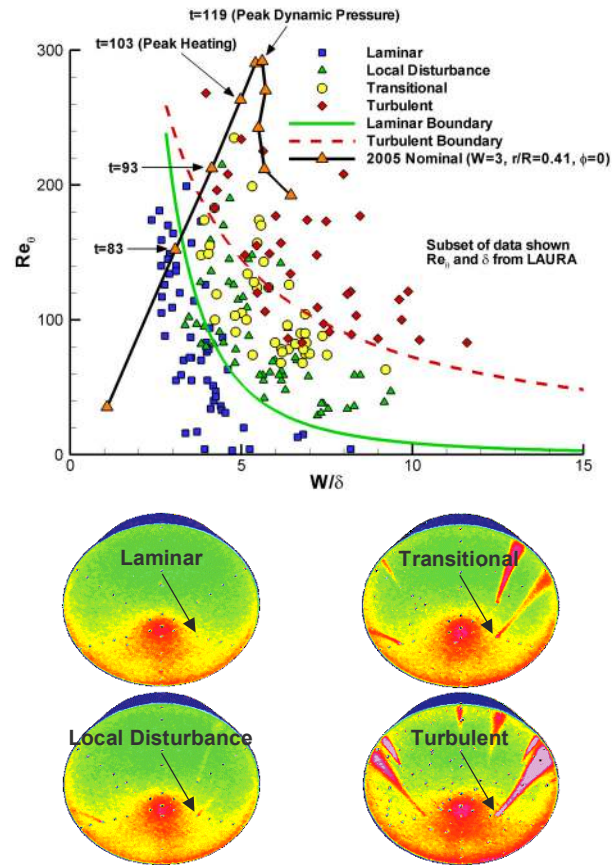

Figure 13. Heatshield Penetrations Transition Map and Legend

It should be noted that using tunnel data to predict transition at flight conditions is a conservative approach. Tunnel noise can accelerate the onset of turbulence, whereas freestream disturbances at flight conditions are generally small. The implications of turbulence on the heating environments are shown next with flight predictions on the nominal trajectory.

Flight Predictions

Two aeroheating quantities are of particular importance for TPS design. First, the selection of candidate TPS materials is limited by the peak heat *rate* encountered during entry. Second, the TPS thickness (and mass) is based on heat rate integrated over the entire heat pulse, or total heat *load*. The effects of turbulence on heat rates and loads were estimated with laminar and turbulent solutions along the nominal trajectory.

Baldwin-Lomax turbulent solutions in a non-equilibrium Mars atmosphere have limitations. First, a user-supplied transition location is required to run the model, and thus is somewhat artificial. Second, the turbulent heat rates predicted during flight are high enough to cause TPS surface recession and pyrolysis, neither of which is factored into the solutions. Nevertheless, the turbulent solutions are believed to be appropriately conservative and are shown to be consistent with the turbulent transition analysis.

Laminar vs. Turbulent Peak Heating

Laminar (LAURA) and turbulent (LAURA and GASP) solutions were obtained at the nominal trajectory peak heating time to compare heating levels and validate results. The transition location for the Baldwin-Lomax solutions was specified at the stagnation point to give fully turbulent heating levels.

A comparison of LAURA laminar and turbulent heat rates is shown in Figure 14 with the $Re_\theta = 200$ level overlaid on the contours. Figure 15 shows a line cut of the data along the symmetry plane. The Baldwin-Lomax solution clearly indicates that turbulence is most effective in augmenting the leeward side heating. The highest laminar heat rate near 37 W/cm^2 occurs on the nose and windward shoulder, and the windward side heating is higher than it is on the leeward side. LAURA predicts a peak turbulent heat rate near 63 W/cm^2 on the *leeward* flank, or about 70% higher than the laminar peak. Some turbulent augmentation is predicted on the windward side, but much less than on the leeward side. This result is consistent with the Re_θ values in those regions.
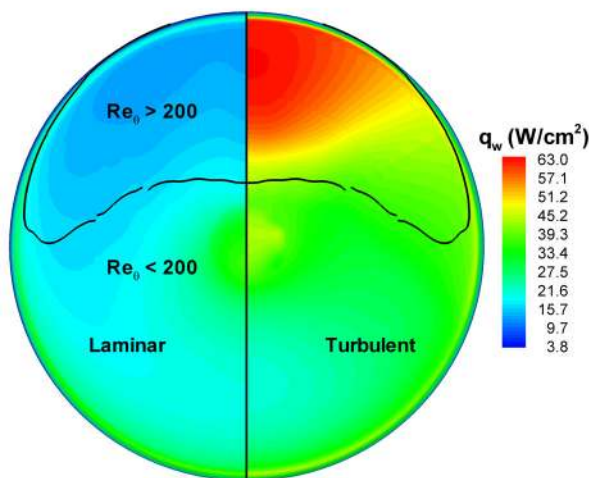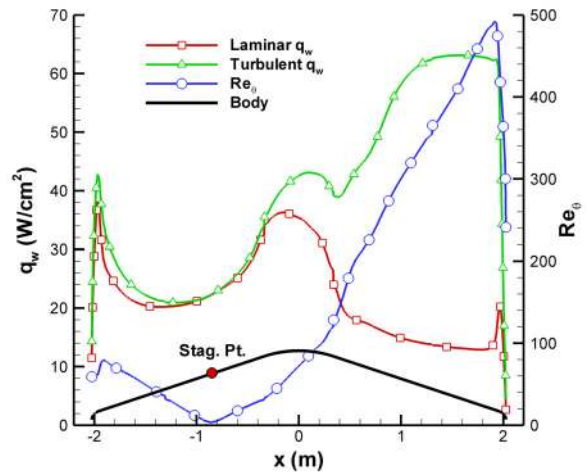
Figure 15. LAURA Symmetry Plane Laminar and Turbulent Heat Rates, and Re_θ at Nominal Peak Heating ($\alpha = 16$ *deg*)

LAURA and GASP turbulent solutions are compared in Figure 16. The GASP solution was run on a different grid than was used with LAURA. Overall, the codes predict heat rates that are within the expected uncertainty of a CFD flight prediction. The important result is that both codes predict the same peak turbulent heat rate near 63 W/cm^2. Differences between LAURA and GASP near the nose are likely due in part to the models used to bridge the laminar and turbulent regions of the flowfield. GASP mimics immediate transition beginning at the user-specified location, whereas LAURA uses the Dhawan-Narashima[32] model to blend the laminar and turbulent regions. Thus, LAURA does not show a rapid rise in heating on the nose like the GASP solution indicates. More importantly, downstream turbulent heat rates agree very well.
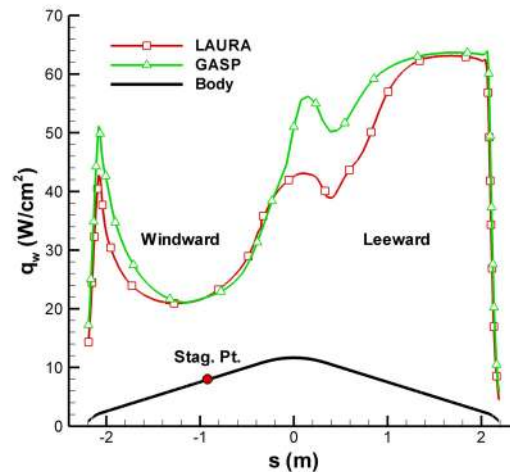
Figure 14. LAURA Laminar and Turbulent Heat Rates, and $Re_\theta = 200$ Contour at Nominal Peak Heating ($\alpha = 16$ *deg*)

Figure 16. LAURA and GASP Symmetry Plane Turbulent Heat Rates at Nominal Peak Heating ($\alpha = 16$ *deg*)

Grid Resolution Study

All LAURA heating predictions are converged for the 7-block grid topology with 64 cells in the surface normal direction. That is, the heating is essentially unchanged with additional grid adaptations. A grid resolution study was conducted to check whether the baseline mesh with 64 normal cells was sufficient to obtain reliable heating predictions. The surface grid distribution was not modified.

Figures 17 and 18 compare LAURA laminar and turbulent solutions at the nominal peak heating point, respectively. Solutions are shown for the reference grid with 64 normal cells and alternate grids with more cells and/or smaller wall spacing. The grid-stretching parameter (ξ_{max}) is the maximum ratio of adjacent cell sizes in the surface normal coordinate direction. Past experience with LAURA has shown that $\xi_{max} > 1.3$ can be excessively large for accurate flowfield resolution.

The laminar solutions with 64 cells ($Re_w = 10$, $\xi_{max} = 1.21$), 80 cells ($Re_w = 10$, $\xi_{max} = 1.16$), and 96 cells ($Re_w = 1$, $\xi_{max} = 1.17$) are virtually identical; the symmetry plane heat rates are within 1% of each other. Figure 18 shows similar agreement for the turbulent solutions using 64 cells ($Re_w = 2$, $\xi_{max} = 1.25$), 80 cells ($Re_w = 2$, $\xi_{max} = 1.19$), and 96 cells ($Re_w = 1$, $\xi_{max} = 1.17$). The grid with 64 normal cells appears to be sufficiently dense for reliable heating predictions at flight conditions while maintaining reasonable grid stretching. Thus, the baseline grid ($Re_w = 10$ for laminar, $Re_w = 2$ for turbulent) was used to run a series of solutions along the nominal trajectory. Smaller wall spacing was used for the turbulent calculations to resolve the relatively thin boundary layer.
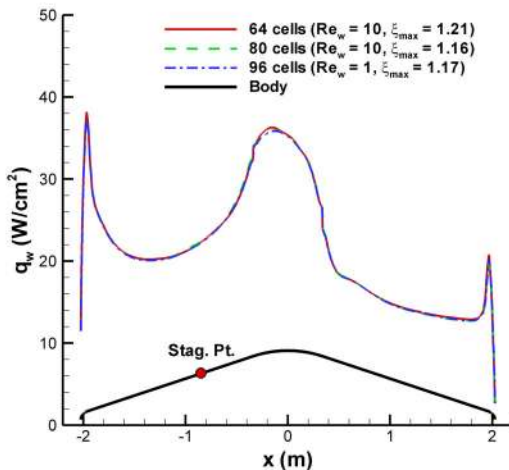

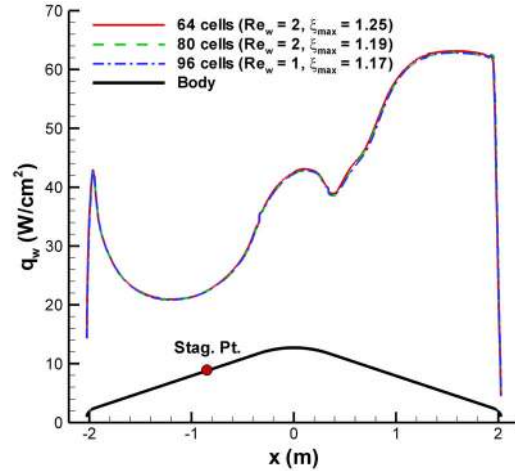**Figure 17. LAURA Laminar Grid Resolution Study at Nominal Peak Heating ($\alpha = 16$ _deg_)**

Figure 18. LAURA Turbulent Grid Resolution Study at Nominal Peak Heating ($\alpha = 16$ _deg_)

Nominal Trajectory Heat Rates

Figure 19 compares LAURA laminar and turbulent symmetry plane heat rate distributions at select times along the nominal trajectory. Turbulent augmentation of the heat rates is evident on the leeside flank for most time points. Virtually no turbulent heating augmentation is predicted at $t = 61$ _s_. However, by $t = 83$ _s_, the turbulent heat rate on the leeward flank is higher than the nose heat rate. A trend of small turbulent augmentation on the windward side and a large heating increase on the leeward side continues through the remaining trajectory points. Turbulent heating augmentation is especially severe at the peak heating ($t = 103$ _s_) and dynamic pressure ($t = 119$ _s_) points.

Table 5 lists the peak laminar and turbulent heat rates for each case shown in Figure 19. Peak Re_θ and turbulent-to-laminar heating ratio are also given for each time. Figure 20 plots the heating ratio and Re_θ data for all CFD solution points. Note that turbulent augmentation, q_{turb}/q_{lam}, is highest at times when Re_θ is large, such as peak heating ($t = 103$ _s_, $Re_\theta = 492$) and peak dynamic pressure ($t = 119$ _s_, $Re_\theta = 576$). At other times when peak Re_θ is lower, but still above the transition criterion of 200, turbulence increases heating by a smaller amount. At $t = 61$ _s_, peak Re_θ is well below the transition criterion and no turbulence augmentation is predicted by the Baldwin-Lomax model. Thus, it appears that the analysis is consistent using a $Re_\theta > 200$ transition criterion in conjunction with the Baldwin-Lomax model to predict turbulent augmentation on a blunt sphere-cone heatshield. However, the Baldwin-Lomax model should not be used to predict transition.
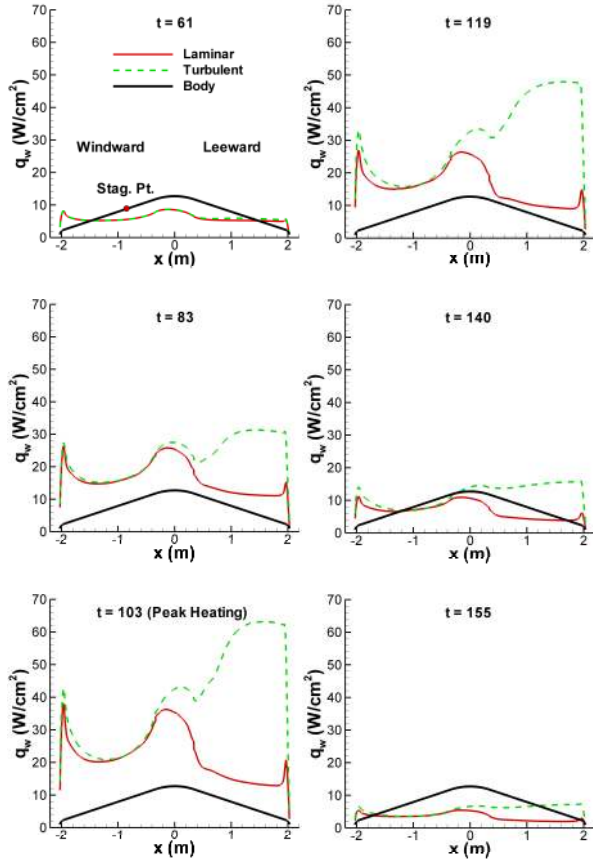
Figure 19. LAURA Symmetry Plane Laminar and Turbulent Heat Rates along Nominal Trajectory (α = 16 *deg*)

Table 5. LAURA Peak Laminar and Turbulent Heat Rates, and Peak Re_θ along Nominal Trajectory (α = 16 *deg*)

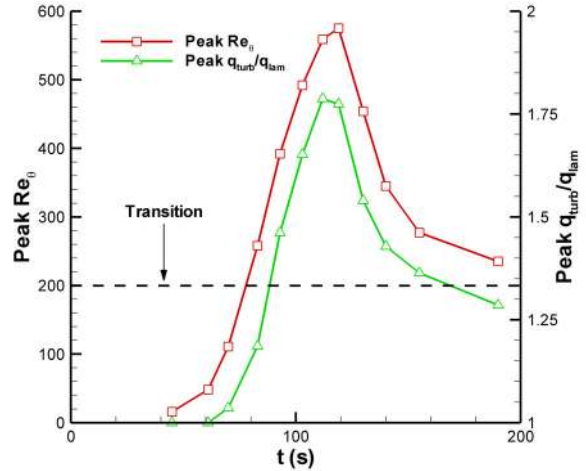| t (s)	Peak q_{lam} (W/cm^2)	Peak q_{turb} (W/cm^2)	Peak q_{turb}/q_{lam}	Peak Re_θ
61	8.6	8.6	1.00	48
83	26	31	1.19	259
103	38	63	1.66	492
119	27	48	1.78	575
140	11	16	1.45	345
155	5.5	7.5	1.36	277

Figure 20. LAURA Peak Re_θ and Heating Ratio along Nominal Trajectory (α = 16 *deg*)

Nominal Trajectory Heat Loads

Figure 21 shows the impact of turbulence on total heat load. The loads are normalized by the laminar nose value of 2570 *J/cm²*. Heat loads are given for three different heat pulses: laminar, turbulent, and an entry with transition at t = 83 *s*. A transition time near t = 83 *s* was estimated for the nominal trajectory. A fully turbulent heat pulse increases the leeside flank heat load to 3540 *J/cm²*, or 38% above the laminar nose value. If transition occurs 20 seconds before peak heating at t = 83 *s*, the peak heat load is 3370 *J/cm²*, or 31% higher than the reference load. Only a 5% reduction in peak heat load occurs on if the heat pulse becomes turbulent at t = 83 *s* versus a fully turbulent pulse. The most conservative approach would be to design a uniform-thickness TPS for the fully turbulent heat pulse.
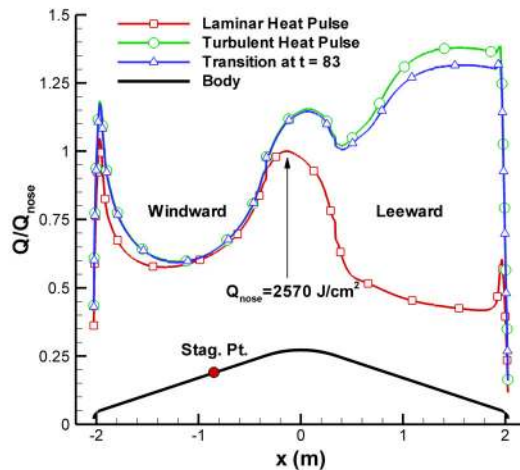

Figure 21. LAURA Symmetry Plane Laminar, Turbulent, and Transitional (t = 83 *s*) Heat Loads along Nominal Trajectory (α = 16 *deg*)

11

The TPS will be designed to the predicted heating environments with additional factors to account for uncertainties in modeling, entry states, atmospheric properties, tunnel-to-flight extrapolation, etc. Some uncertainties are quantifiable, such as entry flight path angle dispersions, while others are less known, such as the extrapolation of tunnel data to flight conditions. The resulting TPS will be a robust and conservative design that is capable of handling worst-case aeroheating environments.

SUMMARY AND CONCLUSIONS

Computational and experimental methods were used to predict forebody aeroheating environments on a proposed Mars Smart Lander aeroshell designed for a hypersonic L/D of 0.22-0.25 ($a = 16$ deg). CFD flight predictions for a direct atmospheric entry from a 2005 launch were computed using an 8-species gas in thermo-chemical non-equilibrium with a radiative-equilibrium wall temperature boundary condition. Laminar and Baldwin-Lomax turbulent solutions were obtained at 12 points along the nominal entry trajectory. CFD was supplemented with wind tunnel tests conducted at NASA LaRC's 20-Inch Mach 6 Air Tunnel to investigate the effects of heatshield penetrations on turbulent transition and heating.

Turbulence was analyzed for both smooth body transition (using a $Re_\theta > 200$ criterion) and transition caused by heatshield cavities. CFD and wind tunnel data predict that both transition mechanisms will cause turbulence on the heatshield leeward flank before the nominal trajectory peak heating point. A peak turbulent heat rate of 63 W/cm^2 is predicted by LAURA and GASP solutions on independent grids; the heat rate is about 70% higher than the laminar peak value. The highest turbulent heating occurs on the heatshield leeward side where Re_θ values are largest. Integrated heat load on the leeward conical flank assuming a fully turbulent heat pulse is 38% higher that the laminar load at the heatshield nose. The peak heat load decreases by only 5% if transition occurs 20 seconds before peak heating versus a fully turbulent heat pulse.

ACKNOWLEDGEMENTS

REFERENCES

1. Lockwood, M. K., Powell, R. W., Graves, C. A., and Carman, G. L., "Entry System Design Considerations for Mars Landers," AAS 01-023, *24th Annual AAS Guidance and Control Conference*, Breckenridge, CO, January-February 2001.

2. Brauer, G. L., Cornick, D. E., and Stevenson, R., "Capabilities and Applications of the Program to Optimize Simulated Trajectories (POST)," NASA CR-2770, February 1987.

3. Cheatwood, F. M. and Gnoffo, P. A., "User's Manual for the Langley Aerothermodynamic Upwind Algorithm (LAURA)," NASA TM-4674, April 1996.

4. *GASP v3.0 User's Manual*, AeroSoft, Inc., 1872 Pratt Drive, Blacksburg VA 24060-6363, 1996.

5. Park, C., Howe, J. T., Jaffe, R. L., and Candler, G. V., "Review of Chemical-Kinetic Problems of Future NASA Missions, II: Mars Entries," *Journal of Thermophysics and Heat Transfer*, Vol. 8, No.1, January-March 1994, pp. 9-23.

6. Papadopoulos, P., Prahbu, D., Olynick, D., Chen, Y. K., and Cheatwood, F. M., "CFD Code Validation and Comparisons for Mars Entry Simulations," AIAA Paper 98-0272, *AIAA Aerospace Sciences Meeting & Exhibit*, Reno, NV, January 12-15, 1998.

7. Queen, E. M., Cheatwood, F. M., Powell, R. W., Braun, R. D., and Edquist, C. T.: ``Mars Polar Lander Aerothermodynamic and Entry Dispersion Analysis,'' *Journal of Spacecraft and Rockets*, Vol. 36, No. 3, May-June, 1999, pp. 421-428.

8. Roe, P. L., "Approximate Reimann Solvers, Parameter Vectors and Difference Schemes," *Journal of Computational Physics*, Vol. 43, No. 2, 1981, pp. 357-372.

9. Yee, H. C., "On Symmetric and TVD Upwind Schemes," NASA TM-86842, September 1985.

10. Baldwin, B. and Lomax, H., "Thin Layer Approximation and Algebraic Model for Separated Turbulent Flows," AIAA Paper 78-0257, 1978.

11. Cheatwood, F. M., and Thompson, R. A., "The Addition of Algebraic Turbulence Modeling to Program LAURA," NASA TM-107758, April 1993.

12. Haas, B. L. and Venkatapathy, E., "Mars Pathfinder Computations Including Base-Heating Predictions," AIAA Paper 95-2086, June 1995.

13. Wercinski, P. F., Henline, W. D., Tran, H., Milos, F., Papadopoulos, P. E., Chen, Y-K., Venkatapathy, E., and Tauber, M. "Trajectory, Aerothermal Conditions, and Thermal Protections System Mass for the Mars 2001 Aerocapture Mission," AIAA Paper 97-0472, January 1997.

14. Prabhu, D. K., Wright, M. J., Marvin, J. G., Brown, J. L., and Venkatapathy, E., "X-33 Aerothermal Design Environment Predictions: Verification and Validation," AIAA Paper 2000-2686, June 2000.

15. Wilke, C. R., "A Viscosity Equation for Gas Mixtures," *Journal of Chemical Physics*, Vol. 18, No. 4, 1950, pp. 517-519.

16. Blottner, F. G., Johnson, M., and Ellis, M., "Chemically Reacting Viscous Flow Program for Multi-Component Gas Mixtures," Sandia National Laboratories, Report SC-RR-70-754, Albuquerque, NM, December 1971.

17. Eucken, A., "On the Heat Conductivity, the Specific Heat, and the Internal Friction of Gases," *Physikalische Zeitscrift*, Vol. 14, 1913, pp. 324-332.

18. van Leer, B., "Flux Vector Splitting for the Euler Equations," ICASE Report 82-30, September 1982.

19. Steinbrenner, J. P. and Chawner, J., "Gridgen's Implementation of Partial Differential Equation Based Structured Grid Generation Methods", *Proceedings, 8th International Meshing Roundtable*, South Lake Tahoe, CA, October 1999, pp. 143-152.

20. Sorenson, R. L. and Alter, S. J., "3DGRAPE/AL: The Ames/Langley Technology Upgrade", *Surface Modeling, Grid Generation, and Related Issues in Computational Fluid Dynamic (CFD) Solutions*, NASA CP-3291, May 1995, pp. 447-462.

21. Alter, S. J., "The Volume Grid Manipulator (VGM): A Grid Reusability Tool", NASA CR-4772, April 1997.

22. Fay, J. A. and Riddell, F. R., "Theory of Stagnation Point Heat Transfer in Dissociated Air," *Journal of the Aeronautical Sciences*, Vol. 25, No. 2, 1958, pp. 73-85.

23. Liechty, D. S. and Hollis, B. R., "Heat Shield Cavity Parametric Experimental Aeroheating for a Proposed Mars Smart Lander Aeroshell," AIAA Paper 2002-2746, *AIAA Fluid Dynamics Conference & Exhibit*, St. Louis, MO, June 2002.

24. Hollis, B. R. and Liechty, D. S., "Boundary Layer Transition Correlations and Aeroheating Predictions for Mars Smart Lander," AIAA Paper 2002-2745, *AIAA Fluid Dynamics Conference & Exhibit*, St. Louis, MO, June 2002.

25. Liechty, D. S. and Hollis, B. R., "Experimental Aeroheating Characteristics for a Proposed Mars Smart Lander," AIAA Paper 2002-4506, *AIAA Atmospheric Flight Mechanics Conference & Exhibit*, Monterey, CA, August 2002.

26. Merski, N. R., Jr., "A Relative-Intensity, Two-Color Phosphor Thermography System," NASA TM-104123, September 1991.

27. Merski, N. R., Jr., "Reduction and Analysis of Phosphor Thermography Data with the IHEAT Software Package," AIAA Paper 98-0712, January 1998.

28. Stetson, K. F., Chapter on "Hypersonic Boundary Layer Transition" in *Advances in Hypersonics: Defining the Hypersonic Environment*, Vol. 1., Editors Bertin, J. J., Periaux, J., and Ballman, J., Birkhauser Boston, Boston, MA, 1992, pp. 324-417.

29. Stetson, K. F., "Boundary-Layer Transition on Blunt Configurations," NASA JSC-26528, February 1994.

30. Mitcheltree, R. A., "Computational Aerothermo-dynamics for Mars Pathfinder Including Turbulence," AIAA Paper 95-3493, *AIAA Atmospheric Flight Mechanics Conference & Exhibit,* Baltimore, MD, August 1995.

31. Cheatwood, F. M., Merski, N. R., Jr., Riley, C. J., and Mitcheltree, R. A., "Aerothermodynamic Environment Definition for the Genesis Sample Return Capsule," AIAA Paper 2001-2889, *AIAA Thermophysics Conference*, Anaheim, CA, June 2001.

32. Dhawan, S. and Narashima, R., "Some Properties of Boundary Layer Flow from Laminar to Turbulent Motion," *Journal of Fluid Mechanics*, Vol. 1, Part 4, January 1958, pp. 418-436.